Numerical modeling and performance enhancement of micro combustor powered thermophotovoltaic systems using high contrast gratings

M V N Surendra Gupta[a,b], Hasan Baig[c], Ameen E[a,b] , Ananthanarayanan Veeraragavan[d], Madan Kumar Lakshmanan[a,e], R I Sujith[f], Bala Pesala[a,e]

[a] Academy of Scientific and Innovative Research, Ghaziabad, Uttar Pradesh, India
[b]CSIR-Structural Engineering Research Center, Chennai, Tamil Nadu, India
[c]Department of Mechanical Engineering, School of Engineering and the Environment, Roehampton Vale Campus, Kingston University, London SW15 3DW, UK
[d]The University of Queensland, School of Mechanical and Mining Engineering, Brisbane, Australia
[e]CSIR- Central Electronics Engineering Research Institute, Chennai, Tamil Nadu India
[f]Department of Aerospace Engineering, Indian Institute of Technology, Madras 600036, India

balapesala@gmail.com

Abstract

Thermophotovoltaic (TPV) systems offer an efficient way to directly convert thermal energy into electricity using the radiation emitted from a high temperature source. Compared to the conventional photovoltaic (PV) systems, TPVs have additional elements such as filters to tailor and shape the radiated energy impinging on the PV cell to improve the conversion efficiency. High contrast grating (HCG) structures are integrated within the combustor walls which act as a selective filter. The filter plays a major role by suppressing the sub-band gap radiation and reflecting it back to the combustion source. Typically, amorphous silicon (a-Si) periodic gratings with quartz as a substrate material are optimized for gallium antimonide (GaSb) PV cells. In this work, we have carried out detailed Multiphysics simulations to study the performance of GaSb, Si and InGaAsSb PV cells when operating in a micro combustor emitting non uniform radiation source operating in a temperature range of 500 – 2000 K. Results show that the proposed TPV system can have a power density of 250 mW/cm^2 using GaSb PV cell. Further, significantly more photons can be converted to useful power with a higher cut-off wavelength PV cell such as InGaAsSb. Therefore, the power density can be as high as 410 mW/cm^2. This study shows that the TPV systems employing low bandgap PV cells can have >20 times higher power density compared to conventional silicon PV cells.

Keywords: Micro-combustor, high contrast gratings, thermophotovoltaics, porous media, solar cell

Highlights:

- Steady-state 3-D modeling is done for parallel plate micro combustor-based TPV system
- Incorporated SiC porous foam enhanced power density by an order of magnitude
- High contrast gratings that are used to tailor the emitted spectral radiation increased power density by 50%
- The reflector is used to confine the power to one side of the micro combustor which doubled the power density

Nomenclature

Symbols

ρ	Density (kg/m^3)	G_m	Mutual irradiation coming from other boundaries (W/m^2)
C_p	Specific heat capacity (J/(kg.K))	G_{ext}	Irradiation from external radiation sources (W/m^2)
T	Absolute temperature (K)	G_{amb}	Ambient irradiation (W/m^2)
u	The velocity vector of translational motion (m/s)	h_{cool}	Convective heat transfer coefficient which represents the effect of exterior cooling (W/(m^2.K))
$\dot{q}$	Heat flux by conduction (W/m^2)	T_{wall}	Combustor wall thickness
$\dot{q}_r$	Heat flux by radiation (W/m^2)	T_{cool}	PV cell back surface temperature (K)
ρ_d	Diffuse reflectivity	$\dot{Q}_{abs}$	Radiation absorbed by the PV cell (W/m^2)
G	Total incoming radiation heat flux (irradiation) (W/m^2)	$r_2.Gm2$	Radiation emitted by the combustor wall in band 2 (0.4 µm – 1.0 µm)
$\dot{Q}$	Additional heat sources (W/m^3)	$r_3.Gm3$	Radiation emitted by the combustor wall in band 3 (1.0 µm – 1.8 µm)
κ	Thermal conductivity (W/(m.K))	Λ	Period the grating (µm)
h	Convective heat transfer coefficient (W/(m^2.K))	a/ Λ	Duty cycle of grating
T_{ext}	External temperature (K)	t$_g$	The thickness of the grating (µm)
ε	Surface emissivity	T$_s$	Input source temperature (K)
σ	Stefan – Boltzmann constant (W/(m^{2}K^4))	FEP	Fractional emissive power
T_{amb}	Ambient temperature (K)	η_{PV}	The efficiency of the PV cell
J	Total outgoing radiative heat flux (radiosity) (W/m^2)	F_{amb}	Ambient view factor
τ	Transmissivity coefficient	ρ_s	Specular reflectivity

1 Introduction

The emitted thermal energy from the heat source has a wide range of temperatures, however the existing combustion mechanical engines systems like gas turbine, rotary engines has high thermal and frictional losses due to its moving parts. In contrast to them, TPV is a static conversion process and operate uninterruptedly, therefore high fuel to electricity conversion can be achieved. Further, the burner/emitter combustion set-up is separated from the actively/passively cooled PV cell, therefore there is no issue of decrease in conversion efficiency due to high temperature radiation. Due to wide range of temperatures, the radiation spectrum should be matched to the bandgap of the PV cell and for efficient conversion by TPV systems. For low-temperature emissions, lower bandgap PV cells can harvest more photons to generate electricity and vice versa. For temperatures above 1300 K, PV cells having wider bandgap such as silicon [1], InGaAs [2], GaSb [3], and for lower temperature less than 1300 K, InGaAsSb alloy lattice-matched on GaSb [4] and InAs [5] have been explored making them more suitable to convert into electricity.

From the beginning of the 2000s, the development of small TPV generators (with powers <10 W) has been accelerating. Several works have been reported on micro combustion-based TPV systems. One of the major concerns is maintaining a good trade-off between the surface to volume ratio and sustaining combustion (as it depends on cube-square law [6]), which otherwise leads to flame quenching. Yang WM et al. [7] reported a micro-TPV system using different kinds of stainless-steel flame tube combustors (a straight tube with and without a sudden expansion step). An average wall temperature of 1300 K was demonstrated.

Further, they have developed an H_2-air combustion system having a volume of 0.113 cm^3. Stable temperature has been obtained for H_2/air ratios varying from 0.45 – 1.0. The system was able to deliver 0.92 W electrical power using GaSb PV cell [8]. In addition, they have proposed that by increasing the backward-facing step height of the micro combustor, higher electrical output power can be obtained [9]. Sui et al. [10] have explored different channel configurations to get optimum temperature uniformity with H_2/air mixtures. Combustion studies are carried out at lean fuel conditions for equivalence ratio in the range of 0.25 – 0.50 for coflow and counter flow configurations. Counterflow configuration has shown a good uniformity in the surface temperature with 19 K standard deviation at maximum surface temperature of up to 1311 K.

As the combustor walls are an essential component of micro-TPV systems, a high and uniform wall temperature is a critical requirement to improve the power output of micro-TPV generators [11]. Therefore, considerable efforts have been made to study various effects on the performance of micro combustors. These include catalytic coatings on the inner surface of walls, different wall configurations (cylindrical and plate type combustors), thickness, and thermal conductivity of walls, etc. Numerical investigations by Pizza et al. [12] demonstrated that the platinum-coated walls could suppress the rich flame dynamics. Zhou et al. [13] have shown experimentally that the micro combustors made of different materials coated with catalyst had

high stability and minimized the radical quenching effect. The combustors have shown high stability until the equivalence ratio of almost zero. For quartz glass and alumina ceramic catalytic micro combustors, the homogenous reaction is stable for the equivalence ratio in the range from $0.0907 - 8.69$ and $0.158 - 7.31$, respectively. Comprehensive investigations have also been done regarding the geometry of the micro combustor. Fan and Wan [14-15] have numerically investigated the micro planar combustor and the effect of length to depth ratio of the cavity. The results have demonstrated excellent stability and expanded the blow-off limit and high flame splitting limit. However, the wall temperature limit decreases. Therefore an optimum length to depth ratio of 3 is recommended for micro combustors with wall cavities.

Almerinda et al. [16] have investigated two different cross-section shapes, square and circular. They showed that in comparison to cylindrical channel, the square cross-section is more resistant to extinction at low inlet velocities. Yang et al. [17] has experimentally studied the cylindrical and planar micro combustors for the equivalence ratio in the range of $0.6 - 1.0$. They have concluded that the planar TPV systems have the advantage of easier fabrication and assembly in comparison to a cylindrical structure. They further studied three kinds of planar combustors with a width of 1.0 mm, 1.5 mm, and 2.0 mm and mentioned that a 1.0 mm geometry has higher radiation efficiency. The heat transfer between the walls and hot gases reduces due to lower wall temperature for larger widths. Lei et al. [18] has numerically studied the effect of wall thickness and material on the stability of the flame. They have pointed out that the micro combustor having thicker and more conductive walls favor a large flame stability limit. Ananthanarayan [19] has proposed an analytical model for a parallel plate micro combustor to study the influence of orthotropic wall materials (higher thermal conductivity in axial and lower in the transverse direction) on the flame speed. The results indicated that thicker walls are better than thinner walls in tailoring thermal conductivity. Kang et al. [20] have experimentally studied the performance of orthotropic walls (using pyrolytic graphite) with anisotropic material (stainless steel). For both the stainless steel and pyrolytic graphite, a stable flame is achieved for the equivalence ratio of $0.8 - 1.25$. They have demonstrated that the orthotropic walls had uniform temperature distribution and had no distinctive hot spot.

The heated combustor walls consequently radiate photons to the surroundings. Among the emitted photons, the photons which have energy higher than the bandgap of the PV cells are converted into usable power. Therefore, achieving high and uniform temperature on the combustor walls leads to intensifying radiative energy. According to Planck's radiation law, it increases the percentage of valuable photons higher than the bandgap (due to improvement in the radiation spectrum). One of the effective methods to improve the power output of micro combustion systems is to insert porous media [21-23]. Chou et al. [24] have numerically studied the performance of micro combustors with and without porous media. The results showed that the porous media enhanced the gas phase combustion. It has increased the heat transferred to the emitter walls from high-temperature combustion products. In addition, the porous media also increases the contact area, leading to high wall temperature, resulting in an enhancement of radiant energy.

Although high radiant energy is obtained, the energy is radiated over a broad range of wavelengths. Therefore, spectral tailoring techniques need to be employed to ensure optimal TPV conversion [25-26]. Kang et al. [27] have used quartz for the combustor walls in the parallel plate micro combustor. Quarts has optical transmission of greater than 85% from near-ultraviolet to mid-infrared region while inhibiting the radiation in the far-infrared region. The results have demonstrated that quartz and porous media have shown better performance with a power output of 121.4 mW for an active emitting area of 625 mm^2. In the cited work [27], for the parallel plate micro combustor configuration, only the studies on the inlet velocity have been demonstrated. However, a comprehensive survey of the effect of various parameters on the parallel plate micro combustor is still missing.

In this work, we have carried out a steady-state 3D modeling of a parallel plate micro combustor that provides a higher wall temperature and exemplary performance in terms of power output. The emitted radiation from the micro combustor is optimized using silicon high contrast grating structures integrated onto combustor walls which act as a selective filter. The filter reflects the sub-bandgap radiation to the combustion source, thereby increasing the combustion efficiency. Due to gratings, the power density of the system has improved by 50%. Owing to its high emissivity, silicon carbide (SiC) porous foam is placed between the combustor walls to improve radiant energy. Further, one of the quartz walls is replaced with a reflector element so that radiation is emitted only on one side of the combustor, which reduces the effective PV cell material needed for TPV conversion. Detailed multiphysics numerical studies for the proposed TPV system is presented in the following sections.

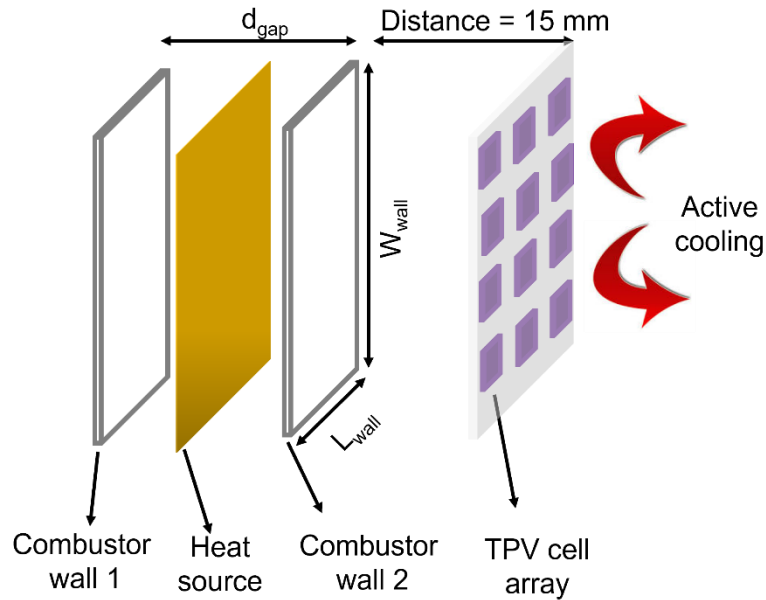# 2 Numerical approach

2.1 Geometric Model

Figure 1: Geometric model of parallel plate micro combustor

The geometric model of the parallel plate micro combustor is shown in *Figure 1*. It consists of two combustor walls separated by 3.5 mm, d_{gap}. The combustor wall's length (L_{wall}) and width (W_{wall}) are 60 mm and 80 mm, respectively. The thickness (T_{wall}) of the combustor walls is 2 mm. To convert the heat radiated from the combustor walls, a photovoltaic (PV) cell is placed, as shown in *Figure 1*. The steady-state 3D modeling is implemented in COMSOL for analyzing the parallel plate micro combustor system. The energy flow diagram is shown in Figure *2*.
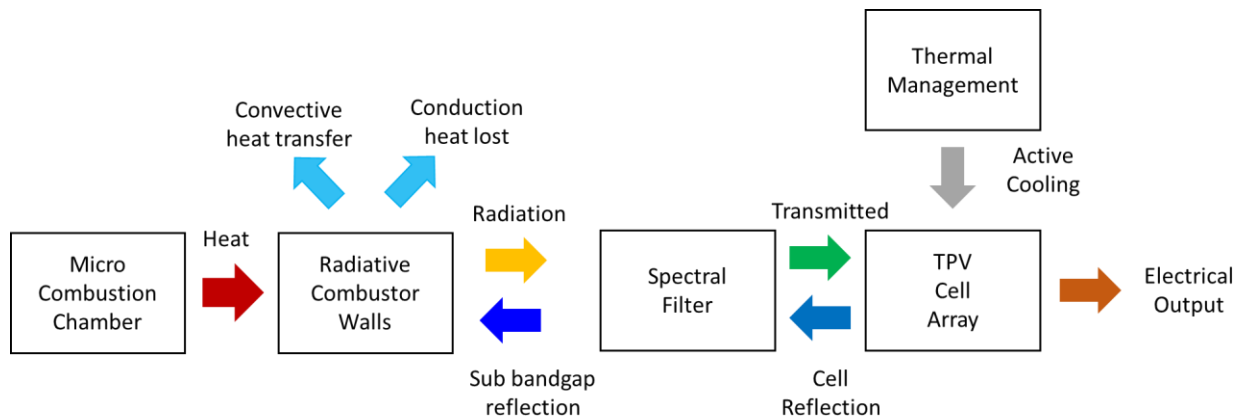

Figure 2: Energy flow diagram for TPV COMSOL model

2.2 Governing equations

The governing equation for the heat transfer in a solid interface is given by Eq. 1.

$$\nabla . \dot{q} + \rho C_p u . \nabla T = \dot{Q} + \dot{Q}_{ted} \tag{1}$$

where ρ is the density, C_p is the specific heat capacity at constant pressure, T is the absolute temperature, u is the velocity vector of translational motion, $\dot{q}$ is the heat flux by conduction, $\dot{Q}$ is the volumetric heat source.

For a continuous medium, the law of heat conduction (Fourier's law) states that the rate of heat transfer which is the conductive heat flux $\dot{q}$ is proportional to the gradient of temperature as defined in Eq. 2.

$$\dot{q} = -\kappa \nabla T \tag{2}$$

where κ is the thermal conductivity.

The governing equation for the heat transfer in a fluid interface is given by Eq. 3.

$$\nabla . q + \rho C_p u . \nabla T = \dot{Q} + \dot{Q}_p + \dot{Q}_{vd} \tag{3}$$

To validate the published results in [27], the temperature profile (extracted from the infrared images of [27]) is given as input on the combustor wall. The governing equation for the temperature on the surface is given by Eq. 4.

$$T = T_o \tag{4}$$

where T_o is the temperature profile obtained from the infrared images.

In the model, the combustor wall exposed to the ambient is defined with both the convective heat flux and surface to ambient radiation boundary conditions.

The convective heat flux coefficient is governed by Eq. 5 and Eq. 6 for the stationary conditions.

$$-n . \dot{q} = \dot{q}_o \tag{5}$$

$$\dot{q}_o = h \left(T_{ext} - T \right) \tag{6}$$

where h is the convective heat transfer coefficient, T_{ext} is the external temperature.

The surface to ambient radiation is governed by Eq. 7.

$$-n . \dot{q} = \varepsilon \sigma (T_{amb}^4 - T^4) \tag{7}$$

where ε is the surface emissivity, σ is the Stefan $-$ Boltzmann constant and T_{amb} is the ambient temperature.

The surface-to-surface radiation physics is used to model the heat transfer between the combustor walls and the PV cell boundary surfaces. The corresponding equation is given by Eq. 8.

$$J = \varepsilon e_b(T) + \rho_d G \tag{8}$$

where J is the total outgoing radiative heat flux (radiosity), ε is the surface emissivity, ρ_d is the diffuse reflectivity, G is the total incoming radiative heat flux or (irradiation).

From Stefan-Boltzmann law, $e_b(T)$ is the power density radiated across all wavelengths, which is given by Eq. 9

$$e_b(T) = n^2 \sigma T^4 \tag{9}$$

where 'n' is the refractive index, σ is the Stefan-Boltzmann constant.

This radiated power is distributed in different wavelength bands, which is given by $r_{i-j}. Gm_n$, where subscript 'n' represents the band number. The normalized spectral irradiance distribution for various temperatures of the blackbody radiation is shown in Figure *3*.
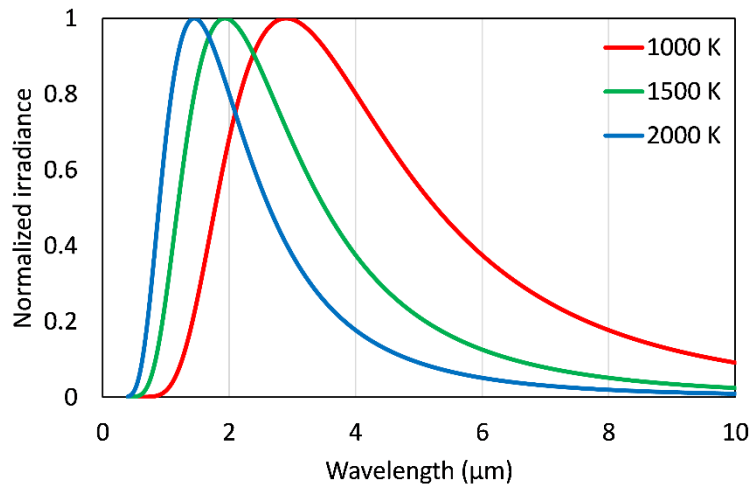

Figure 3: Normalized spectral irradiance of the blackbody for the temperature 1000 K, 1500 K, and 2000 K

The total incoming radiative flux G is given by Eq. 10

$$G = G_m(J) + G_{amb} + G_{ext} \tag{10}$$

where G_m is the mutual irradiation coming from other boundaries in the model, G_{ext} is the irradiation from external radiation sources and G_{amb} is the ambient irradiation.

The ambient irradiation G_{amb} is given by Eq. 11

$$G_{amb} = F_{amb} e_b(T_{amb}) \tag{11}$$

where F_{amb} is the ambient view factor.

The ray shooting method of surface-to-surface radiation physics is used with a wavelength-dependent radiative property. A semi-transparent surface with multiple spectral bands is considered to account for the combustor wall's reflection, transmission, and emission. The governing equation is given by Eq. 12.

$$\varepsilon_i + \rho_{d,i} + \rho_{s,i} + \tau_i = 1 \tag{12}$$

where ε_i is the surface emissivity, $\rho_{d,i}$ is the diffuse reflectivity, $\rho_{s,i}$ is the specular reflectivity and τ_i is the transmissivity.

Therefore, the total outgoing radiative heat flux Eq. 8 is modified to Eq. 13

$$J_i = \varepsilon_i e_b(T) FEP_i(T) + \rho_{d,i} G_i \tag{13}$$

where FEP is the fractional emissive power and is given by Eq. 14

$$FEP_i(T) = \frac{15}{\pi^4} \int_{\frac{c2}{\lambda_{i-1}T}}^{\frac{c2}{\lambda_i T}} \frac{x^3}{1 - e^x} dx \tag{14}$$

Figure 4 shows the TPV cell arrangement consisting of 5 TPV cells connected in parallel vertically and 5 such blocks connected horizontally in series. This configuration will be helpful as the flame temperature will have significant variation along the combustor surface in the vertical direction. For the PV cell front surface, the diffuse surface properties are chosen with a boundary heat source. The PV cells convert a fraction of irradiation to electricity instead of heat. Heat sinks on the inner boundaries simulate this effect by accounting for a boundary heat source, $\dot{q}$, defined by Eq. 15

$$\dot{q} = -G\eta_{PV} \tag{15}$$

where η_{PV} is the efficiency of photovoltaic cells and is given by Eq. 16 [29].

$$\eta_{PV} = \begin{cases} 0.2\left[1 - \left(\frac{T}{800\ K} - 1\right)^2\right], & T \leq 1600\ K \\ 0 & , & T > 1600\ K \end{cases} \tag{16}$$
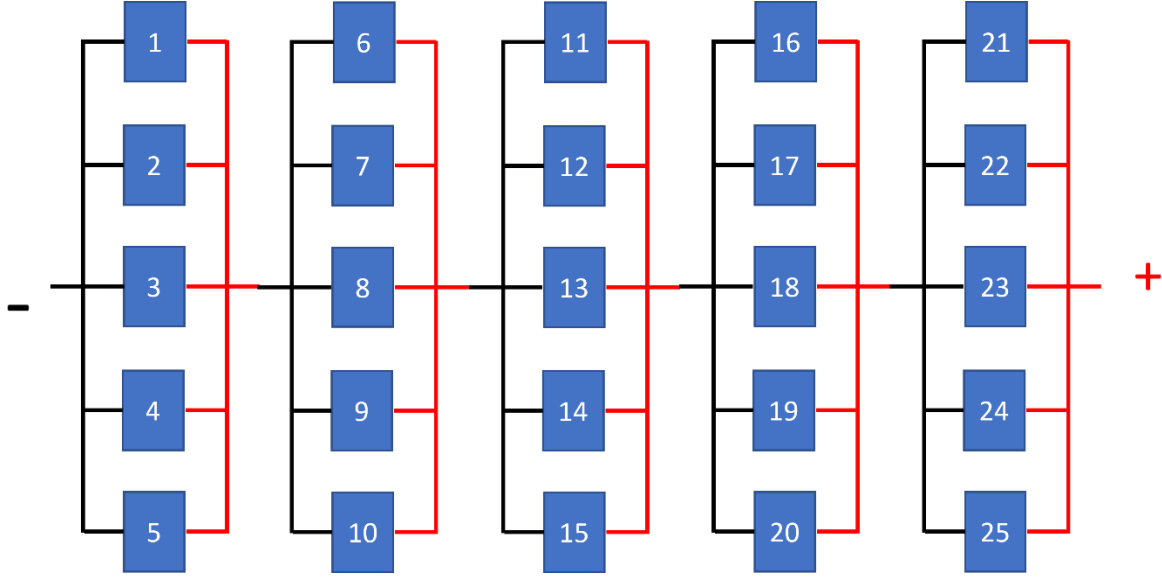
9

Figure 4: TPV cells arrangement. Five cells are connected in parallel vertically, and five such blocks are connected horizontally in series.

For cooling purposes, the back surface of the PV cell is given a boundary heat source condition to dissipate the heat at a rate provided by Eq. 17.

$$\dot{Q}_b = h_{cool} * (T_{cool} - T) \tag{17}$$

where h_{cool} is convective heat transfer coefficient which represents the effect of exterior cooling and T_{cool} is the temperature at which the backside boundary surface of the PV cell is to be maintained.

2.3 Validation of numerical simulation

Here, the experimental results of Kang et al. [27] have been considered to validate the developed numerical model. In the experiments, silicon wafers of size 60 mm x 80 mm are used as combustor walls. The material properties of the silicon are given in *Table 1*.

Table 1: Material properties of Silicon and PV cell

Property	Silicon	PV cell
Thermal conductivity, κ	131 W/(m.K)	93 W/(m.K)
Density, ρ	2329 kg/m³	2400 kg/m³
Heat capacity at constant pressure, Cp	700 J/(kg.K)	80 J/(kg.K)

The transmissivity, reflectivity, and emissivity for silicon are not the same at all wavelengths. Therefore wavelength-dependent radiative properties are taken as shown in *Table 2*. which is obtained from the ref. [29-30].

Table 2: Wavelength dependent spectral properties of silicon

Band	Wavelength region	Transmissivity	Reflectivity	Emissivity
1	< 0.4 μm	0.00	0.35	0.50
2	0.4 μm – 1.0 μm	0.00	0.35	0.60
3	1.0 μm – 1.8 μm	0.40	0.45	0.65
4	> 1.8 μm	0.50	0.50	0.65

The convective and radiative heat transfer from the silicon combustor wall is given by Eq. 18

$$Q = h_o * (T_{wall} - T_o) + \varepsilon\sigma(T_{wall}^4 - T_o^4)$$

(18)

where h_o is the natural convective heat transfer coefficient. Typical values of h_o are in the range of $2 - 25$ W/(m².K) [31]. Therefore, here h_o of 5 W/(m².K) is considered. As the combustors are tested in the atmosphere, T_o is taken as 298 K.

The gap between the combustor wafers is 3.5 mm and is filled with the air-fluid in the numerical model. And further, the gap between the combustor wall and the PV cell is 15 mm, which is also filled with air-fluid. The properties of the PV cell are given in *Table 1*. As mentioned, to account for cooling the back surface of the PV cell, a boundary heat source condition is used to dissipate the heat provided by Eq. 17. The convective heat transfer coefficient h_{cool} is taken as 50 W/(m².K) [32 - 33] and the temperature T_{cool} is 273.15 K.

The IR image from [27] as the temperature profile on the silicon combustor wall surface is shown in *Figure 5*a. The shape of the temperature of the 3D structure is shown in Figure 5b. From the combustor surface the emitted radiation is as shown in Figure 5c. GaSb PV cells can only convert the radiation in the band range of 0.4 μm – 1.8 μm to helpful power. The radiation emitted in the remaining bands will not be absorbed by the PV cell as the external quantum efficiency is zero [34]. The temperature profile on the PV cell is shown in Figure 5d.
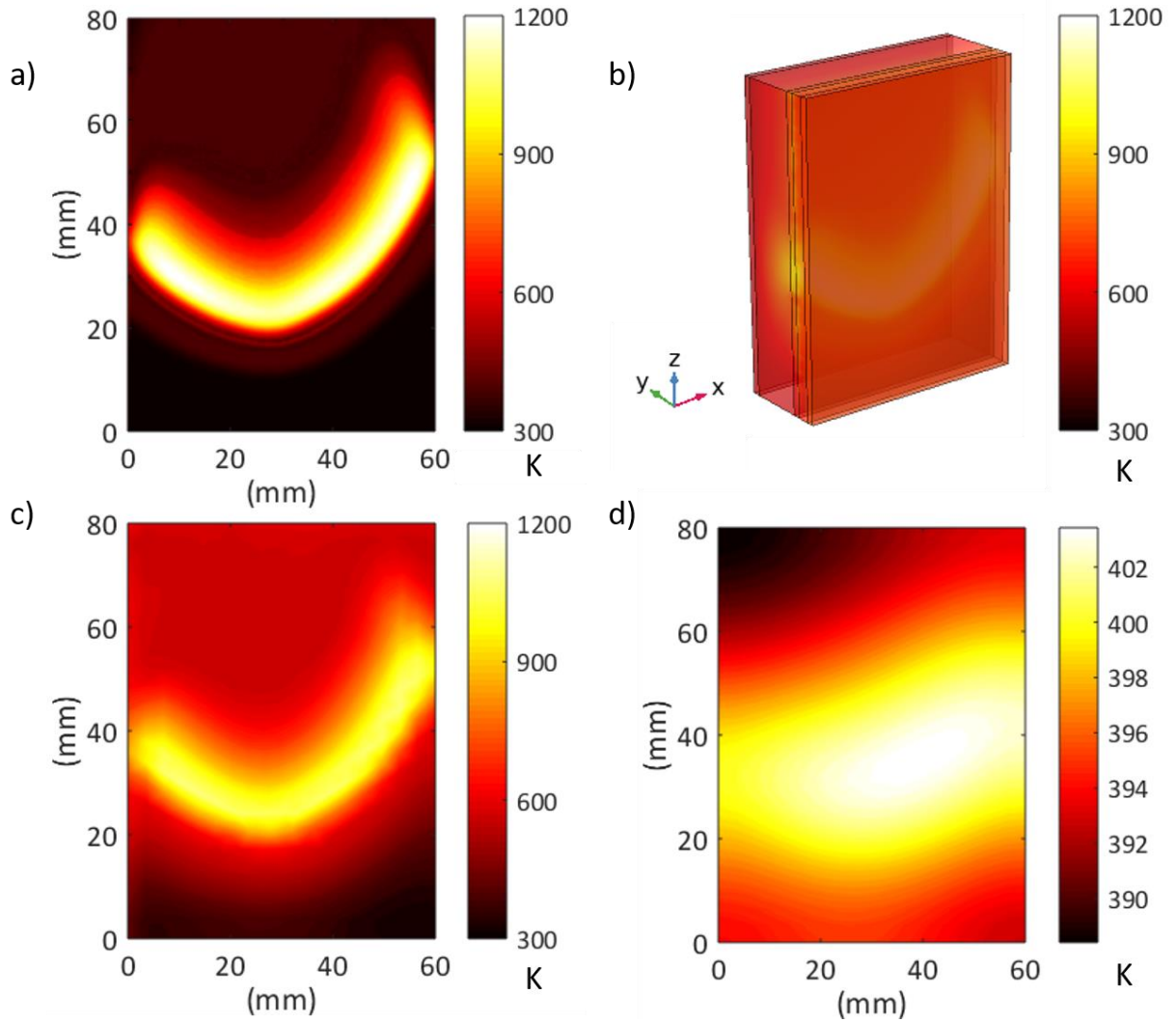
Figure 5: a) Temperature profile for the input source obtained from the IR image of Ref [27] b) 3D contour profile of temperature c) Temperature profile on the combustor wall surface d) Temperature profile on the PV cell surface

The radiation that is absorbed by the PV cell is given by Eq. 19.

$$Q_{abs} = (r_2 . Gm2 + r_3 . Gm3) * \eta_{PV}$$

(19)

where $r_2 . Gm2$ and $r_3 . Gm3$ are the radiation emitted by the combustor walls in band 2 (0.4 μm – 1.0 μm) and band 3 (1.0 μm – 1.8 μm) respectively and η_{PV} is the efficiency of the PV cell. The obtained results show that the cumulative power density in band 2 and band 3 is 8.10 W/m². The area of the PV cell used in [27] is 37 cm². Therefore, the power output is 29.5 mW which is in close agreement with the reported power of 27.6 mW. In addition, the measurement accuracy of the power is ±1.8% of the experimental results. Figure 6 shows the validation of the experimental data with the numerical simulation for various source temperatures. Therefore,

good agreement between the results of experiments and simulation indicates the reliability and accuracy of the developed numerical model.
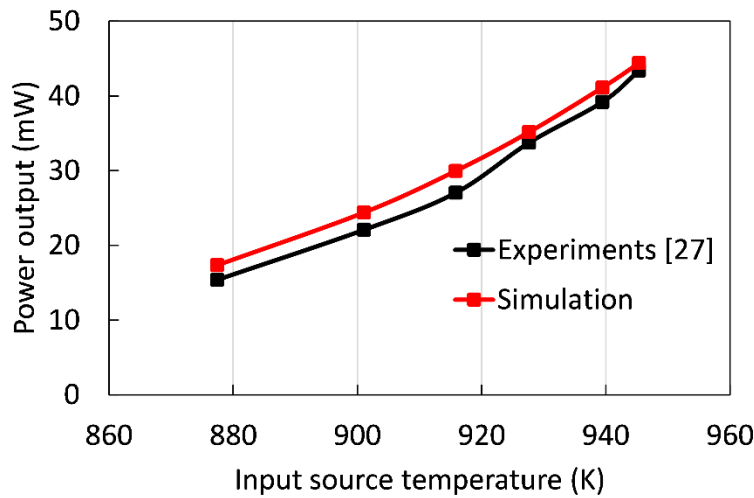

Figure 6: Validation of experimental data with numerical simulation for various source temperatures

2.4 Grid independent study

The numerical solution should ensure that the obtained simulation results are independent of grid resolution. Hence, the rectangular micro-combustor is simulated for different mesh resolutions ranging from highly coarse (with domain elements of 517) to finer (with domain elements of 42,232), as shown in *Figure 7*. With the continued increase in the mesh resolution, the numerical solution converges to a stable value. The accuracy of the mesh is determined by verifying the change in the results obtained with the current mesh accuracy to the previous mesh accuracy. If the precision is sufficient, it excludes the need for computationally finer grid simulations. Here, the output power has almost remained the same from domain elements of 16,473 till the finer resolution using 42,232 elements. The difference in the power output is <0.7% between the fine (with domain elements of 27,837) and finer resolution studies. Therefore, all the studies are performed using fine resolution, beyond which the solution shows appreciable grid independence.
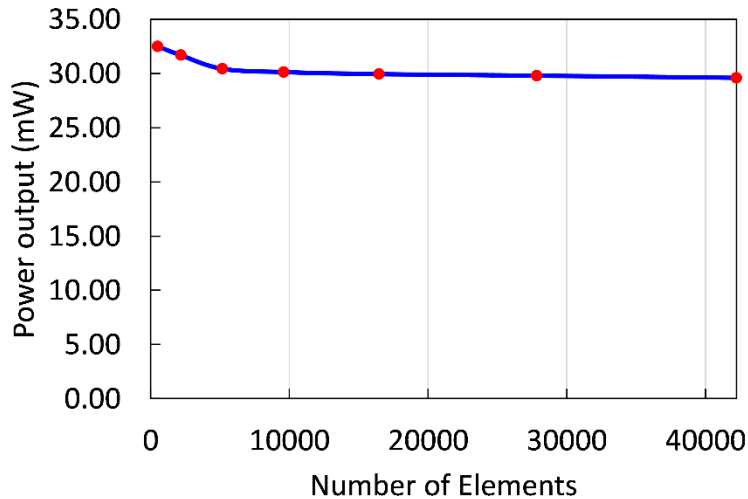
Figure 7: Mesh sensitivity study - a variation of power output with several elements

3 High contrast gratings for TPV

Apart from the TPV as a portable power generator using micro combustors, these systems also have potential applications for waste heat recovery [35-37]. The latest research is focused on improving the efficiency of the TPV systems by tailoring the spectral shape of the radiation using selective emitters and filters. Figure *8* shows the schematic of the operating principle of TPV with the integration of spectrally selective components. Selective emitters are designed to emit photons in a particular wavelength band, either in a very narrow band [38] or in a broadband region [39 - 40]. Silva-Oelker et al. [41] have designed a planar multilayer stack composed of tungsten and hafnia layers with high emittance in the wavelength region of $0.4 - 1.8$ µm suitable for GaSb PV cells having an efficiency of 27.1%. Lenert et al. [42] have fabricated a broadband emitter using alternating layers of Si/SiO_2 suitable for InGaAsSb PV cells and demonstrated a conversion efficiency of 3.2%. Although broadband emitters result in increased power being incident on the PV cell, the high energy photons above the bandgap of the PV cell result in thermalization losses hence lowering the PV conversion efficiency.

In [51], narrowband emitters are explored to emit radiation in a very narrow wavelength region. This is done to have an emissivity of one in the narrow region of wavelength and a zero emissivity elsewhere. However, such narrowband emitters result in less power, and therefore a balance between the power and efficiency is required to make better use of selective emitters. Further, these structures radiate in all directions providing no control on the directionality of emission. Grating structures and metamaterials allow control of the emitted radiation both spectrally and directionally [44 - 45].

Further, the integration of spectral filters inhibits the sub-bandgap radiation and allows only the convertible photons onto the PV cell, thus reducing the thermalization losses that deteriorate

14

the PV cell efficiency. In addition, the reflected sub-bandgap radiation promotes photon recycling, thus increasing the system performance. Rahmlow et al. [46] used Al_2O_3 substrates to fabricate front surface tandem filters, which suppressed the below bandgap radiation. Bierman et al. [47] fabricated a tandem plasma-interference filter that stopped 80% of sub-bandgap photons and PV cell conversion efficiency of 6.8%.
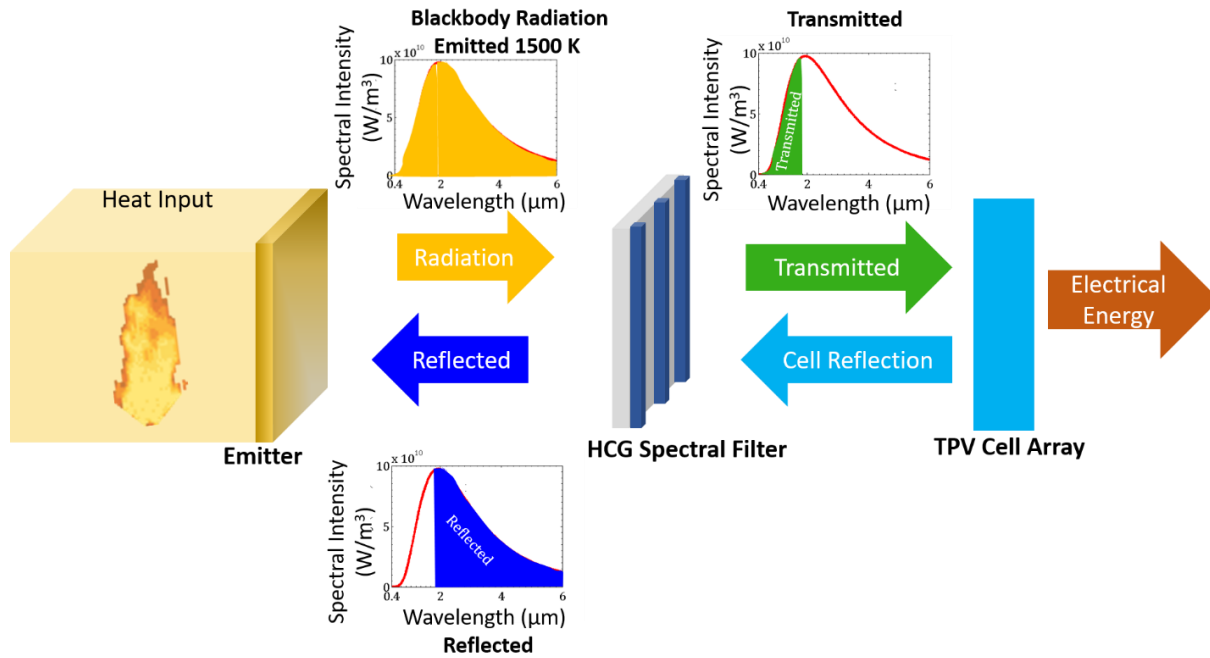

Figure 8:High contrast gratings as a spectral filter for TPV

Several grating-based structures are explored for spectral and directional control of the emitted radiation [48-49]. Chen and Zhang [50] have optimized to have maximum emittance in the wavelength band of 0.4 – 1.8 µm (suitable for GaSb PV cell) using 1D simple and complex tungsten gratings (combination of the short-period grating (Λ =0.4 µm) and long-period grating (Λ=1.6 µm). In our previous study [51], we have designed and fabricated a one-dimensional high contrast grating (HCG) infrared filter. Several materials, such as Si_3N_4, TiO_2, and a-Si, were explored to realize an infrared filter suitable to the GaSb PV cell. *Figure 9* shows the HCG-based filter's schematic using amorphous silicon as a grating material on a quartz substrate.
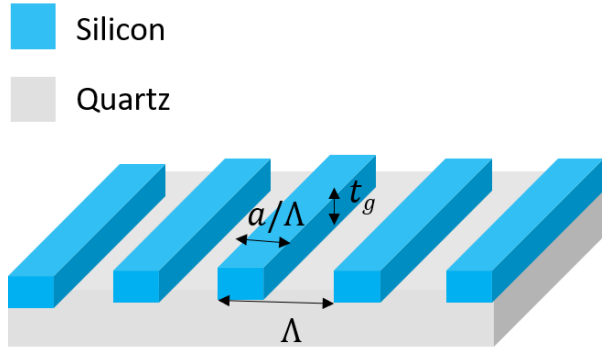
Figure 9: One-dimensional high contrast amorphous silicon gratings on a quartz substrate

Simulations are optimized using the Rigorous Coupled Wave Analysis technique in Grating Solver Development Co. software (Gsolver V5.2) to inhibit the transmission of the sub-bandgap photons by optimizing the grating parameters. The bandgap wavelength for the GaSb PV cell is 1.8 µm. Therefore radiation above 1.8 µm is not convertible by the GaSb PV cell. Quartz, because of its inherent nature, does not allow the transmission above 4.5 µm. In comparison, gratings parameters (period (Λ) = 2.4 µm, duty cycle (a/Λ) = 0.4 and thickness (t_g) = 600 nm) are optimized to inhibit the transmission above 1.8 µm further. Therefore, the filter reflects the radiation above 1.8 µm and contributes to increased source temperature due to photon recycling. The transmission contour plot for the period = 2.4 µm, duty cycle = 0.4 for various thicknesses is shown in Figure *10*a. At a thickness of 0.6 µm, the transmission above 1.8 µm is almost minimal, and the corresponding transmission spectrum of the optimized HCG filter is shown in *Figure 10*b.
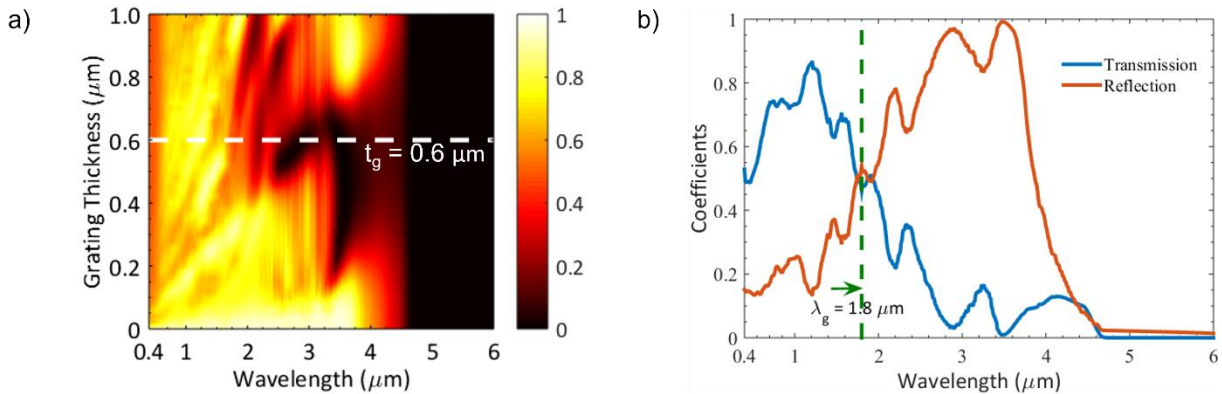

Figure 10: a) Contour plot of transmission spectrum for grating period Λ = 2.4 µm and DC = 0.4. b) Transmission, reflection and absorption spectrum of the optimized HCG filter with a grating thickness of 0.6 µm.

Figure 10 shows that the photons in the wavelength region, 1.8 µm to 4.8 µm, are reflected back to the source. This will contribute to the enhancement in the combustion leading to an increase in the quartz wall temperature, resulting in higher electrical power output. In the next section, the parametric study simulations are carried out by integrating the HCG filter onto the quartz walls of the developed micro-combustor model, and the performance enhancement is evaluated for various configurations.

4 Results and discussion

The parametric studies consider a uniform heat source for various temperatures, as combustion modeling is not a part of this work. However, for non-uniform temperature distribution sources where the flame has either a convex or concave shape, the power output will be higher than the uniform sources [27].

4.1 Effect of input heat rate

The rectangular micro-combustor is studied for various input temperatures of the source ranging from 500 K to 2000 K. For these studies the combustor walls are taken as quartz substrates. The material properties are given in *Table 3*.

Table 3: Material properties of quartz

Property	Quartz
Thermal conductivity, κ	10.7 W/(m.K)
Density, ρ	2600 kg/m^3
Heat capacity at constant pressure, Cp	710 J/(kg.K)

Since the transmission, reflection and emission are wavelength-dependent for the quartz substrate, the wavelength-dependent radiative properties considered for simulation [28] are shown in *Table 4*.

Table 4: Wavelength dependent spectral properties of quartz

Band	Wavelength region	Transmissivity	Reflectivity	Emissivity
1	< 0.4 µm	0.5	0.15	0.35
2	0.4 µm – 1.8 µm	0.8	0.15	0.05
3	1.8 µm – 2.8 µm	0.8	0.15	0.05
4	2.8 µm – 4.0 µm	0.45	0.15	0.40
5	> 4.0 µm	0.0	0.15	0.85

The output power density is evaluated for each input temperature value within the wavelength range absorbed by the GaSb PV cell. As a GaSb PV cell absorbs only in the wavelength range of 0.4 µm – 1.8 µm, the power is calculated for the band 2 region defined in *Table 4*. *Figure 11*a shows the graph of output power density obtained for the given input source temperature. From Planck's law, the spectral emissive power 'W' from an object (in W/m^2/µm) is given by Eq. 20:

$$W(\lambda, T) = \varepsilon(\lambda, T) . \frac{2\pi h c^2}{\lambda^5 [\exp\left(\frac{hc}{\lambda kT}\right) - 1]}$$

(20)

where ε is the emissivity of the object, T is the temperature, λ is the wavelength, k is the Boltzmann constant (1.381 x 10^{-23} J/K) and h is the Planck constant (6.626 x 10^{-34} J.s)
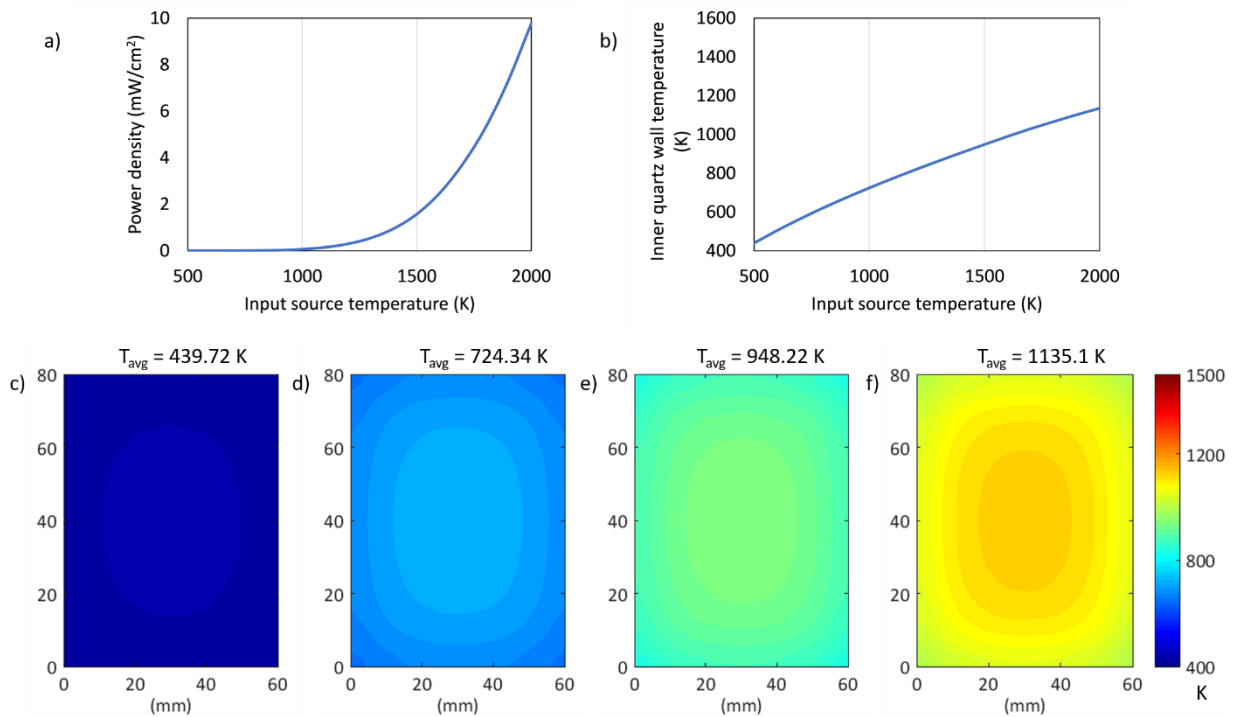

Figure 11: Effect of input temperature on output power density. a) Input source temperature vs Power density. b) Input source temperature vs inner quartz wall temperature. c) Input source temperature (T_s) = 500 K. d) Input source temperature (T_s) = 1000 K. e) Input source temperature (T_s) = 1500 K f) Input source temperature (T_s) = 2000 K

*Figure 11*b shows the inner quartz wall temperature for the given input source temperature. As the input source temperature increases, the internal quartz wall temperature increases and the corresponding power output. The surface temperature profile of the inner quartz wall is shown in *Figure 11*c, *Figure 11*d, *Figure 11*e, and *Figure 11*f for the input source temperature (T_s) of 500 K, 1000 K, 1500 K, and 2000 K having an average surface temperature of 439.72 K, 724.34 K, 948.22 K, and 1135.1 K respectively.

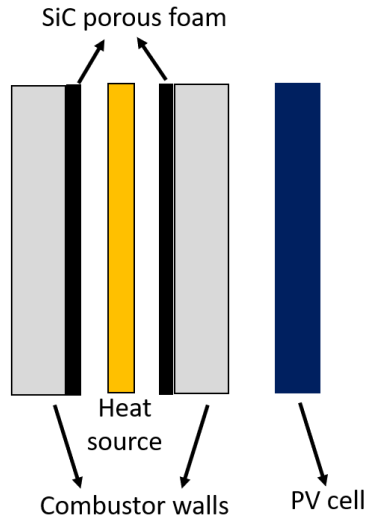## 4.2   Effect of porous media material

Figure 12: Porous foam inserts on the combustor walls

One of the effective methods to improve the power output of TPV is by using porous media material in micro-combustion [22-23]. The porous media material has strong thermal interaction with the flame, i.e., it can store the heat and therefore reduces heat losses from the combustor surface. A high emissivity foam also increases the radiated power that can be captured by the solar cell. Due to this, the quartz wall combustor temperature will rise to a very high temperature leading to the emission of high energy photons for increased power output. Further, the porous media also stabilizes the flame and extends the flammability limit. The configuration of the porous foam inserts on the combustor walls is shown in Figure *12*. The material properties used for the SiC porous material for the numerical modeling are shown in *Table 5*. The thermal conductivity of the SiC varies with the temperature. Therefore a cubic spline interpolation was used for fitting the thermal conductivity in the temperature range of 500 K – 2000 K.

Table 5: Material properties of SiC porous foam [27]

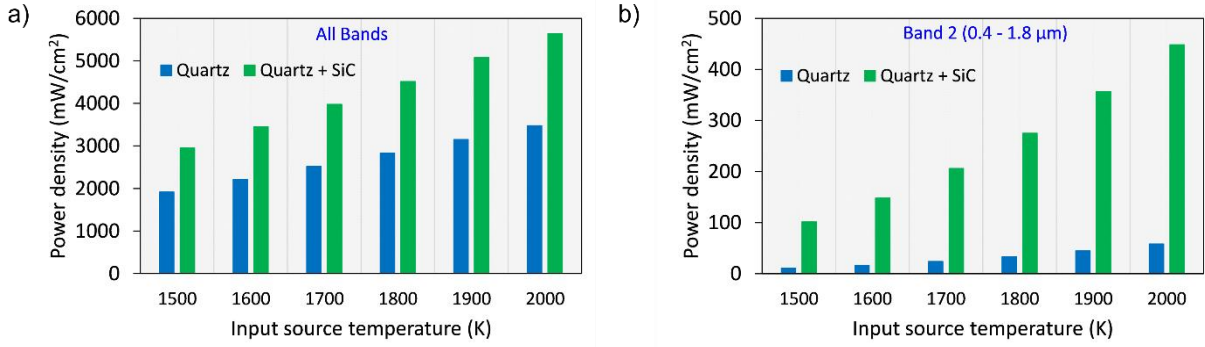| Property	SiC porous material	
Surface emissivity	0.95	
Density, ρ	3200 kg/m³	
Heat capacity at constant pressure, Cp	1000 J/(kg.K)	
Porosity	100 PPI (pores per inch)	
Thermal conductivity	523 K	5.28 W/m.K
	1273 K	1.85 W/m.K
	1723 K	1.34 W/m.K

Figure 13: Improvement in the power density due to incorporation of porous material. a) All Bands. b) Band 2

The power from the band 2 that is convertible by PV cell into useful power is given by Eq. 21

$$P = A_{SiC} . \tau_{Qz} . \varepsilon_{SiC} \int_{0.4\ \mu m}^{1.8\ \mu m} \frac{2\pi hc^2}{\lambda^5 [\exp\left(\frac{hc}{\lambda k T_{SiC}}\right) - 1]} d\lambda \qquad (21)$$

where A_{SiC} is the emitting area of SiC porous foam, τ_{Qz} and ε_{SiC} denote the transmissivity and emissivity of the quartz and SiC porous foam, respectively.

Figure *13* shows the improvement in the power density for the temperature range of $1500 - 2000$ K with and without the SiC porous foam. Figure *13*a shows the total power density combined in all the bands, and Figure *13*b is for band 2 ($0.4 - 1.8$ µm), where the emitted radiation is converted by the PV cell into helpful power. It can be observed that there is an improvement in the power density almost by an order of magnitude due to the high emissivity of the SiC porous foam and because of its strong thermal interaction with the heat source. *Figure 14*a shows the power density output for the given input source temperature ranging from 500 K – 2000 K. Compared to Figure 11a, Figure 14a shows a higher output power for the same input source temperature. This is due to the higher inner quartz wall temperature due to SiC porous material shown in Figure 14b compared to Figure 11b. The surface temperature profile of the inner quartz wall is shown in Figure 14c, Figure 14d, Figure 14e, and Figure 14f for the input source temperature of 500 K, 1000 K, 1500 K, and 2000 K having an average surface temperature of 457.64.72 K, 775.73 K, 1010.70 K, and 1190.00 K respectively. On comparing *Figure 11*f and *Figure 14*f, i.e., for the input source temperature of 2000 K, the surface temperature has increased by 55 K, and the power density has improved by 71 mW/cm^2 due to porous foam incorporation.
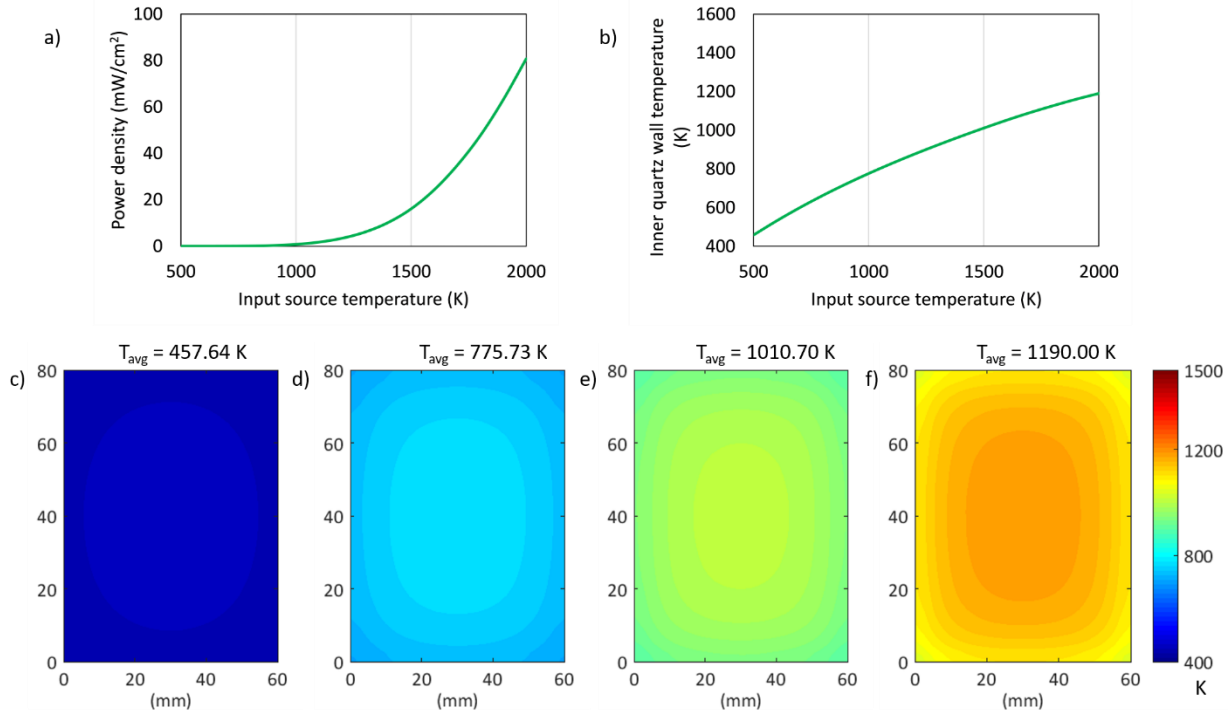
Figure 14: Effect of porous media material. a) Input source temperature vs Power density. b) Input source temperature vs inner quartz wall temperature. c) Input source temperature (T_s) = 500 K. d) Input source temperature (T_s) = 1000 K. e) Input source temperature (T_s) = 1500 K. f) Input source temperature (T_s) = 2000 K

Though the SiC porous foam improves the combustion by holding the heat, it emits a broad range of wavelengths. Due to sub-bandgap and thermalization losses, the PV cell will not effectively convert the entire radiation into helpful electricity. Therefore, the spectral tailoring structures need to be integrated to tailor the radiation emitted from the combustor to match the solar cell band absorption optimally.

4.3 Effect of high contrast grating-based spectral filters

High contrast gratings integrated into the quartz combustor walls tailor the spectral radiation emitted from the combustor. *Figure 9* shows the one-dimensional amorphous silicon-based high contrast grating structure on a quartz substrate. The design is optimized to inhibit the sub-bandgap radiation that is not absorbed by the GaSb PV cell, as observed from the transmission and reflection spectrum of *Figure 10*. The wavelength-dependent spectral properties shown in *Table 6* are given on the outer surface of the quartz walls in the numerical model.

Table 6: Wavelength dependent spectral properties of HCG structure

Band	Wavelength region	Transmissivity	Reflectivity	Emissivity
1	< 0.4 μm	0.50	0.20	0.30
2	0.4 μm – 1.8 μm	0.75	0.20	0.05
3	1.8 μm – 2.8 μm	0.20	0.75	0.05

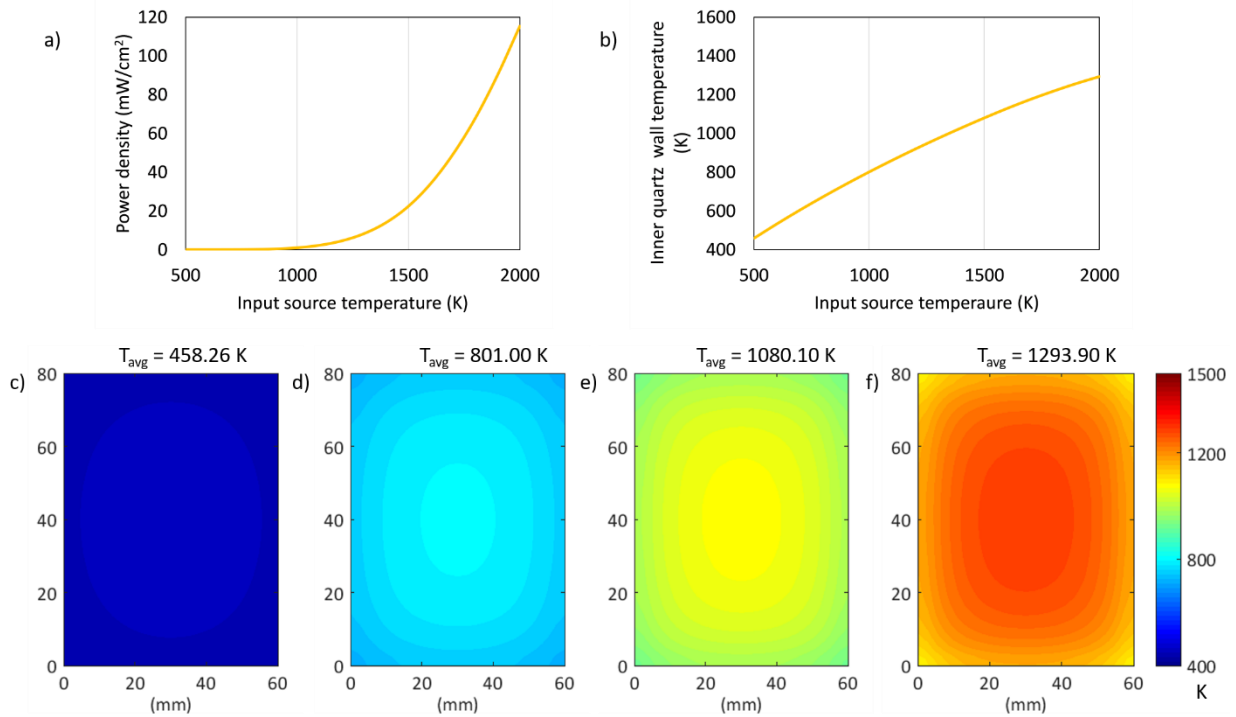| 4 | 2.8 µm − 4.0 µm | 0.10 | 0.85 | 0.05 |
| 5 | > 4.0 µm | 0.00 | 0.10 | 0.90 |

Figure 15:Effect of high contrast gratings. a) Input source temperature vs Power density. b) Input source temperature vs inner quartz wall temperature. c) Input source temperature (T$_s$) = 500 K. d) Input source temperature (T$_s$) = 1000 K. e) Input source temperature (T$_s$) = 1500 K. f) Input source temperature (T$_s$) = 2000 K

Figure 15a shows the output power density of the PV cell for the given input source temperature range of 500 K – 2000 K. In comparison to Figure *14*a, the power density output shown in Figure *15*a has increased by approximately 1.5 times. This increment in power output is due to the increase in temperature of the combustor wall (shown in Figure *15*b) due to the reflection of sub-bandgap energy from being transmitted. To show the effect of the high contrast gratings, the power density in the band 2 (0.4 µm – 1.8 µm), band 3 (1.8 µm – 2.8 µm), and band 4 (1.8 µm – 4.0 µm) are shown in Figure *16* and compared it with the previous case of quartz + SiC. It can be observed that the power density in band 3 (Figure *16*b) and band 4 (Figure *16*c) of quartz + SiC + HCG are decreased due to the reflection of sub-bandgap photons by the HCG structure, which contributed to the increase in the band 2 (Figure *16*a) power density. Therefore, HCG plays a significant role in the up-conversion of low-energy photons and enhances the combustion leading to high wall temperature resulting in increased power output. The surface temperature profiles of the quartz wall are shown in Figure *15*c, Figure *15*d, Figure *15*e, and Figure *15*f for the input source temperature of 500 K, 1000 K, 1500 K, and 2000 K having an average surface temperature of 458.26 K, 801.00 K, 1080.10 K, and 1293.90 K respectively.
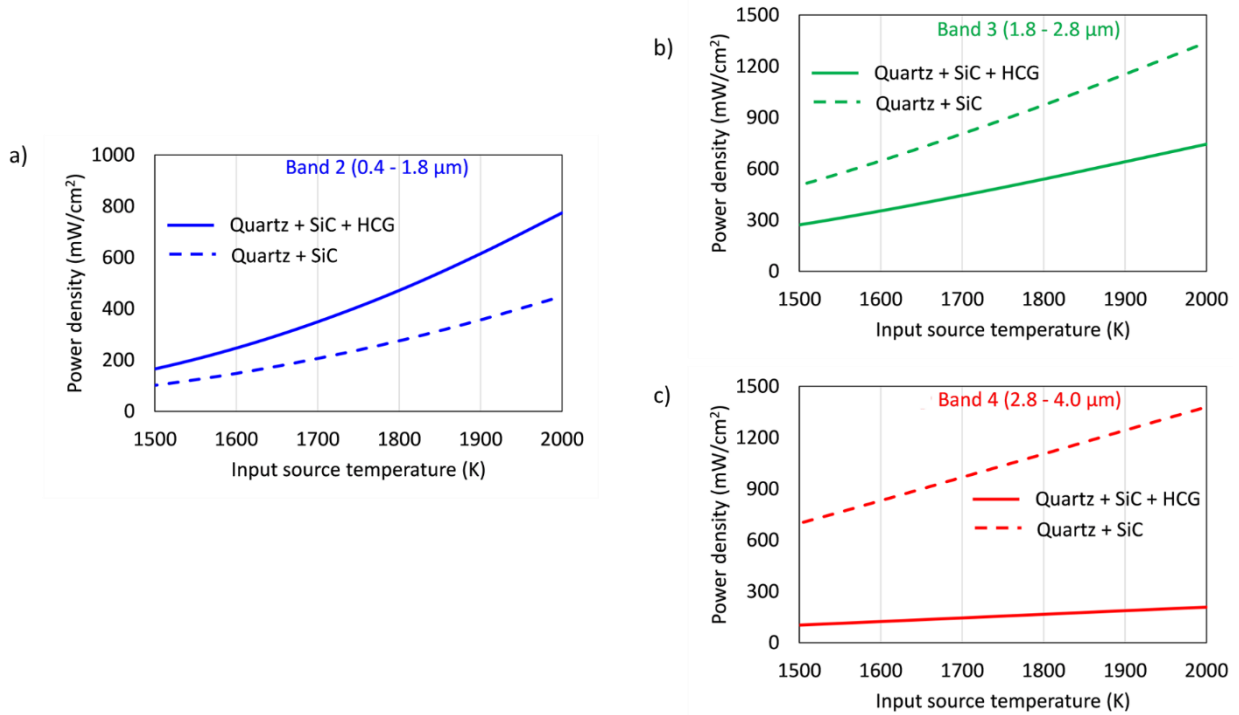
Figure 16: Distribution of radiation power density. a) Band 2 (0.4 – 1.8 μm). b) Band 3 (1.8 – 2.8 μm). c) Band 4 (2.8 – 4.0 μm)

4.4   Effect of replacing one of the combustor walls with a reflector
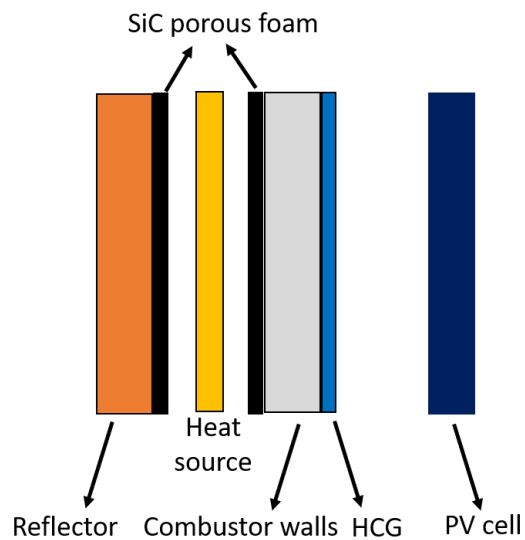

Figure 17: Schematic representation of the numerical model replacing one of the quartz combustors walls with the metal reflector

The developed numerical model uses a parallel plate combustor using quartz as combustor walls on both sides. Therefore, power is radiated on both sides, and an additional PV cell needs to be used to capture the radiation on the other side of the combustor. Instead, to avoid the usage of

supplementary PV cell material, a metal reflector element is placed, replacing one of the quartz walls so that the total power will be radiated onto one side of the combustor, as shown in Figure 17. The material properties of the reflector used in the modeling are shown in *Table 7*.

Table 7: Material properties of reflector [52]

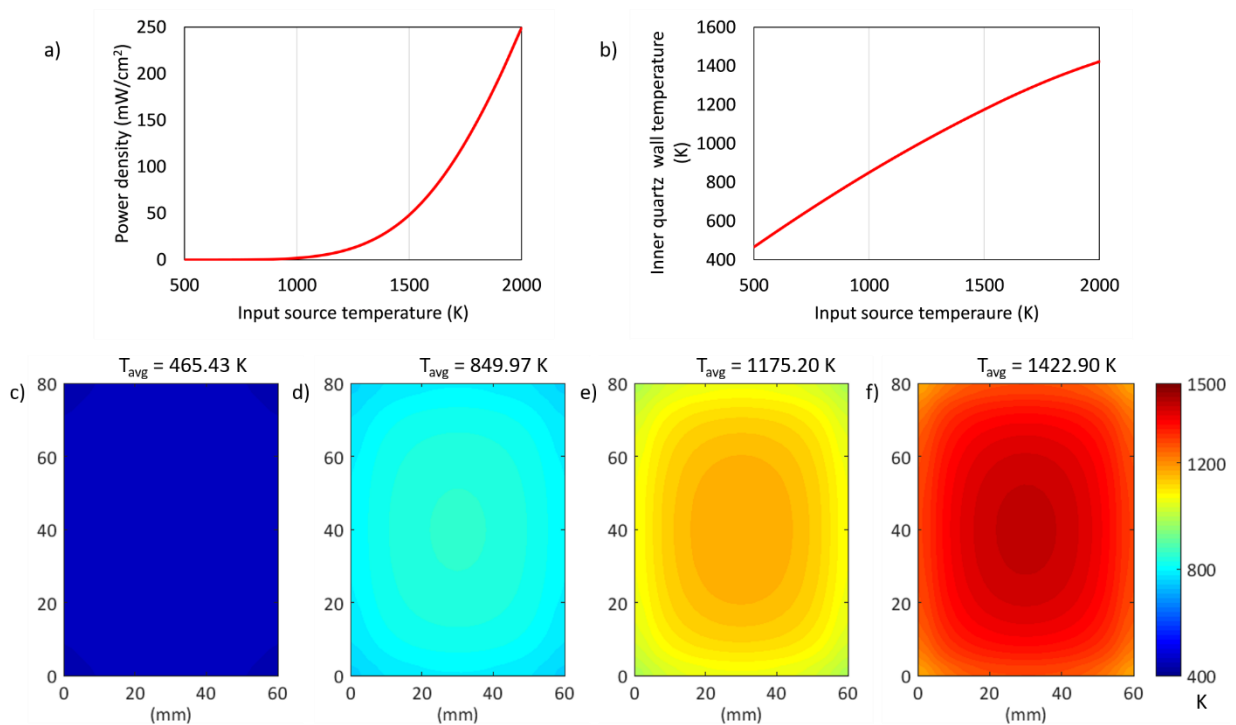| Property	Reflector
Thermal conductivity, κ	10.0 W/(m.K)
Density, ρ	5000 kg/m^3
Heat capacity at constant pressure, Cp	840 J/(kg.K)
Surface emissivity	0.01

Figure 18:Effect of reflector element. a) Input source temperature vs Power density. b) Input source temperature vs inner quartz wall temperature. c) Input source temperature (T_s) = 500 K. d) Input source temperature (T_s) = 1000 K. e) Input source temperature (T_s) = 1500 K. f) Input source temperature (T_s) = 2000 K

Figure *18*a shows the power density output for the given input source temperature ranging from 500 K – 2000 K. It can be observed that in comparison to Figure *15*a, the power obtained with the reflector has doubled. This is due to the reflector element blocking the radiation from emitting from the other side of the combustor. Therefore, the combustor wall temperature and radiative efficacy on one side increase (as shown in Figure 17b), leading to increased power output. For a temperature of 2000 K, the output power density is 249.5 mW/cm^2 (Figure *18*a) in comparison to 115.4 mW/cm^2 (Figure *15*a) without the reflector element. This is due to an increase in the quartz wall temperature by 130 K. The surface temperature profiles of the quartz

wall are shown in Figure *18*c, Figure *18*d, Figure *18*e, and Figure *18*f for the input source temperature of 500 K, 1000 K, 1500 K and 2000 K having an average surface temperature of 465.43 K, 849.97 K, 1175.20 K, and 1422.90 K respectively.

4.5 Overall enhancement of micro combustor TPV system

Beginning with the basic configuration of quartz-based parallel plate micro combustor, the methods to improve TPV power output are explored by using SiC porous foam, high contrast grating structures, and reflector elements. The overall improvement in the power output and the increase in the temperature is shown in Figure *19*. For the temperature of 2000 K, the TPV power is 9.8 mW/cm^2 (only quartz), 80.8 mW/cm^2 (quartz + SiC), 115.4 mW/cm^2 (quartz + SiC + HCG) and 249.5 mW/cm^2 (quartz + SiC + HCG + reflector), i.e. an improvement factor of 25 (Figure *19*a) which is due to the increase in the quartz wall temperature and improved radiative efficacy out of the combustor (Figure *19*b).
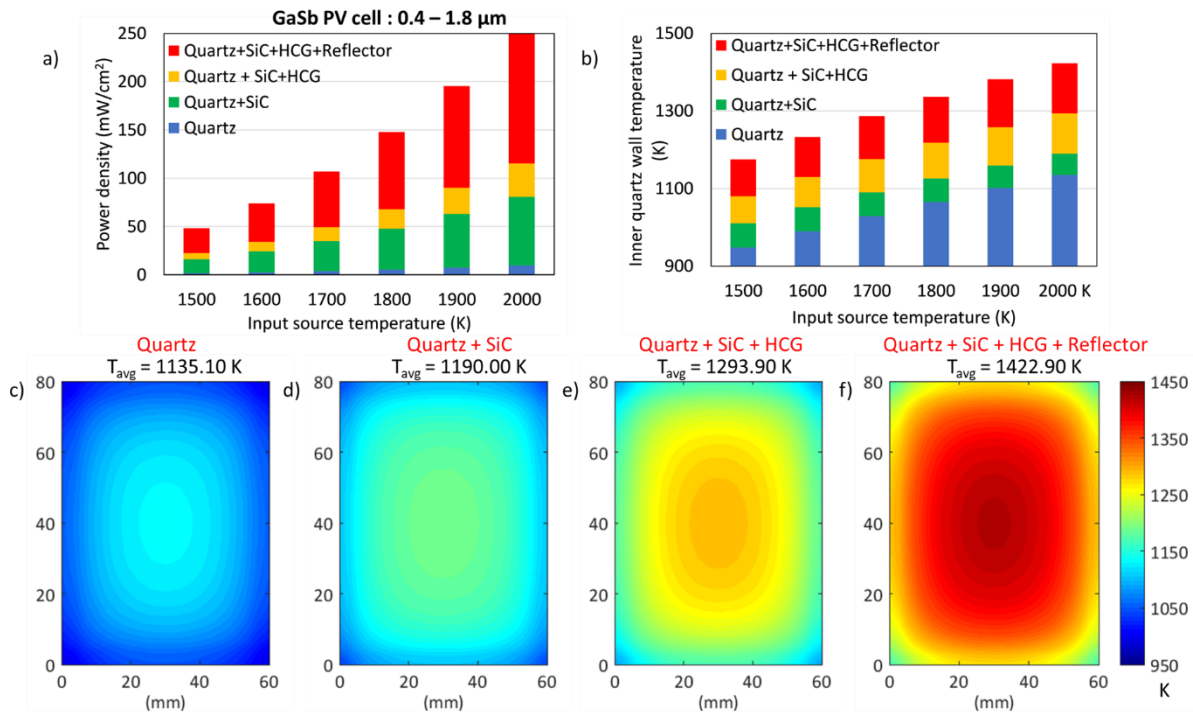

Figure 19: Overall enhancement of the micro combustor TPV system due to incorporation of SiC porous material, HCG gratings and reflector element. a) Input source temperature vs Power output. b) Input source temperature vs inner quartz wall temperature. c) Quartz (T_s)= 2000 K. d) Quartz + SiC (T_s) = 2000 K. e) Quartz + SiC + HCG (T_s) = 2000 K. f) Quartz + SiC + HCG + Reflector (T_s) = 2000 K

The surface temperature profile for the four configurations is shown in Figure *19*c, Figure *19*d, Figure *19*e, and Figure *19*f having a maximum temperature of 1135 K (only quartz), 1190 K (quartz + SiC), 1294 K (quartz + SiC + HCG) and 1423 K (quartz + SiC + HCG + reflector) respectively, i.e., an increase in temperature by 288 K. The efficiency of the TPV system is calculated using Eq. 22 and its variation with respect to the temperatutre is shown in Figure *20*.

$$\eta_{TPV} = \frac{P_{out}}{Q_h} \tag{22}$$

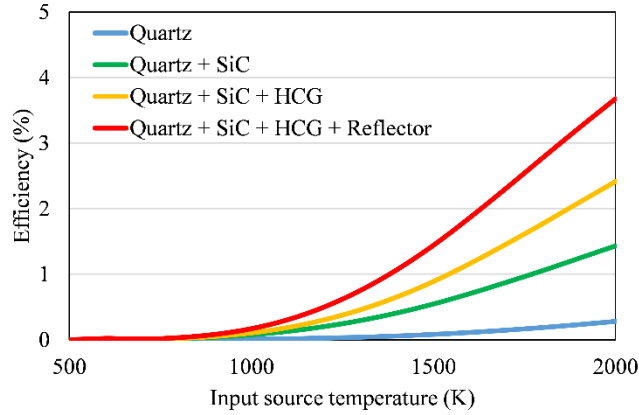where P_{out} is the generated electrical power and Q_h is the heat flow out of the combustor wall surface.

Figure 20:Variation of efficiency with respect to the temperature for GaSb PV cell

The efficiency results achieved are consistent with the published studies by Chan et.al [53] Lenert et.al [54]. Further, the power density is obtained from the developed numerical model for higher bandgap Si and lower bandgap InGaAsSb PV cells. The Si PV cell has a cut-off wavelength of approximately 1.1 μm. For the maximum temperature of 2000 K simulated in this model, the fraction of total power within bandgap range of 0.4 – 1.1 μm (convertible band) is <10% as compared to >50% for InGaAsSb in the convertible range of 0.4 – 2.2 μm, i.e., reduced by a factor of 4 times. Figure *21*a shows the power density obtained for all four cases for Si PV cells. Similarly, Figure *21*b shows the power density for InGaAsSb, which has a cut-off wavelength of 2.2μm. A significantly greater number of photons can be converted to useful power by the PV cell since the cut-off wavelength for the InGaAsSb PV cell is higher than the Si PV cell. Therefore a power density of 410 mW/cm^2 sat 2000 K is obtained for Quartz + SiC + HCG + Reflector. It should be noted that the potential power density realized from the micro-combustor-based TPV systems using low bandgap materials is at least a factor of 20 times (~400 mW/cm^2) compared to conventional solar-powered based systems (~20 mW/cm^2). Further, the efficiencies with Si and InGaAsSb PV cell are calculated and shown in Figure *21*c and Figure *21*d, respectively. Thus the combustor-based TPV systems are an attractive option for applications requiring high power density.
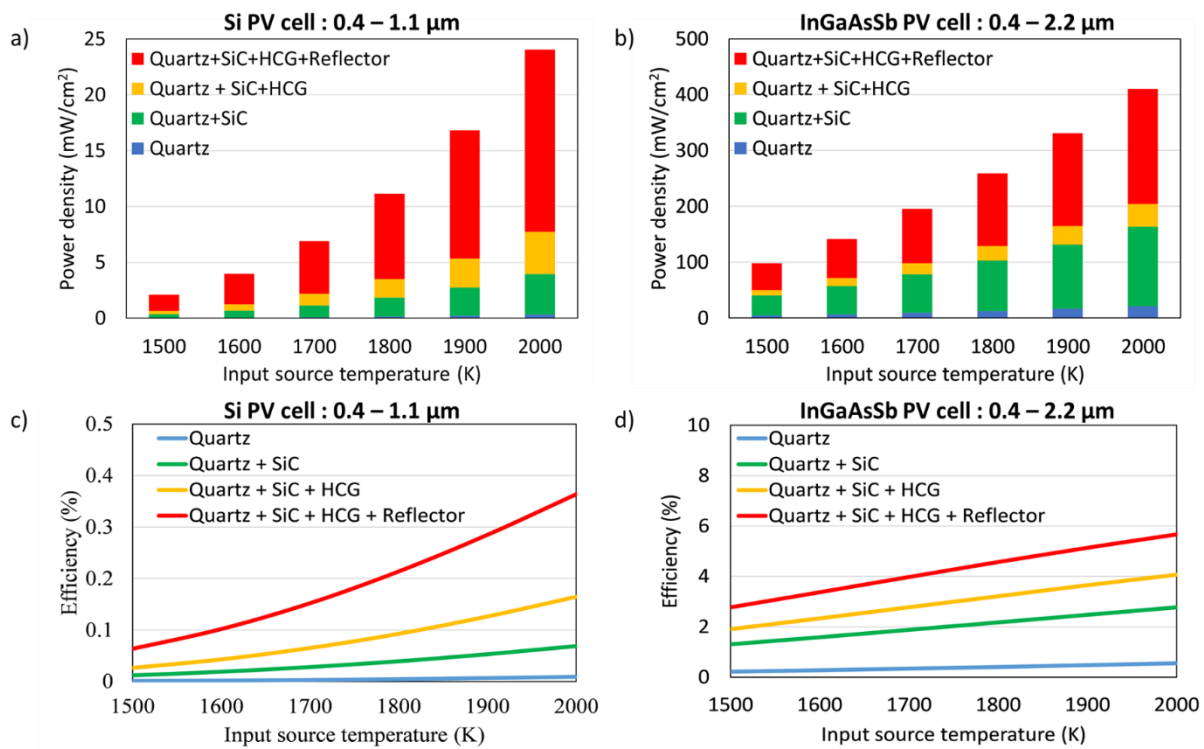
Figure 21: Power density vs. Input source temperature. a) Si PV cell. b) InGaAsSb PV cell. Efficiency vs. Input source temperature. C) Si PV cell d) InGaAsSb PV cell

5 Conclusions

- In this work, a steady-state three-dimensional heat transfer modeling is done for a parallel plate micro-combustor along with a PV cell. The modeling is done by considering all the material properties of the combustor walls, PV cell, SiC porous foam, high contrast grating, and reflector surface.

- The developed model is validated with the reported literature of the parallel plate micro combustor and further explored different techniques to improve the power and the efficiency of the TPV system.

- Parametric analysis is carried out by varying the input source temperature. The output power is evaluated for each of the cases: Quartz, Quartz + SiC, Quartz + SiC + HCG, and Quartz + SiC + HCG + Reflector.

- With the incorporation of porous foam, the combustion is enhanced, leading to higher wall temperature and approximately eight times improvement in the power output.

- HCG structure optimized for tailoring the radiation spectrum by inhibiting the sub-bandgap radiation and converting it into higher energy photons for improving the power density in the convertible region. Due to this, the power is enhanced by 1.5 times in comparison with quartz + SiC.

- The addition of a reflector to one side of the combustor wall has doubled the output power compared to quartz + SiC + HCG.
- Simulations are carried out for various solar cells, Si and InGaAsSb. For Si PV cells with a higher bandgap, the maximum density is 24 mW/cm^2. For lower bandgap InGaAsSb PV cells, the maximum power density obtained is 410 mW/cm^2 since more photons are converted to useful power by InGaAsSb. Therefore, TPV systems employing low bandgap materials can have significantly higher power density > 20 times compared to a conventional solar photovoltaic system using Si PV cells.

Acknowledgments

References

1. Bitnar B, Durisch W, Grutzmacher D, Mayor JC, Muller C, Von Roth F, Selvan JA, Sigg H, Tschudi HR, Gobrecht J. A TPV system with silicon photocells and a selective emitter. In Conference Record of the Twenty-Eighth IEEE Photovoltaic Specialists Conference-2000 (Cat. No. 00CH37036) 2000 Sep 15 (pp. 1218-1221). IEEE.
2. Tan M, Ji L, Wu Y, Dai P, Wang Q, Li K, Yu T, Yu Y, Lu S, Yang H. Investigation of InGaAs thermophotovoltaic cells under blackbody radiation. Applied Physics Express. 2014 Aug 28;7(9):096601.
3. Bett AW, Sulima OV. GaSb photovoltaic cells for applications in TPV generators. Semiconductor science and technology. 2003 Apr 4;18(5):S184.
4. Dashiell MW, Beausang JF, Ehsani H, Nichols GJ, Depoy DM, Danielson LR, Talamo P, Rahner KD, Brown EJ, Burger SR, Fourspring PM. Quaternary InGaAsSb thermophotovoltaic diodes. IEEE Transactions on Electron Devices. 2006 Nov 30;53(12):2879-91.
5. Lu Q, Zhou X, Krysa A, Marshall A, Carrington P, Tan CH, Krier A. InAs thermophotovoltaic cells with high quantum efficiency for waste heat recovery applications below 1000 C. Solar Energy Materials and Solar Cells. 2018 Jun 1;179:334-8.
6. Menon S, Cadou C. Investigation of performance scaling in small internal combustion engines. InEastern states section meeting of the combustion institute, Charlottesville, VA 2007 Oct 21.
7. Yang WM, Chou SK, Shu C, Xue H, Li ZW, Li DT, Pan JF. Microscale combustion research for application to micro thermophotovoltaic systems. Energy conversion and management. 2003 Sep 1;44(16):2625-34.

8. Yang WM, Chou SK, Shu C, Xue H, Li ZW. Development of a prototype micro-thermophotovoltaic power generator. Journal of Physics D: Applied Physics. 2004 Mar 17;37(7):1017.

9. Yang WM, Chou SK, Shu C, Li ZW, Xue H. Experimental study of micro-thermophotovoltaic systems with different combustor configurations. Energy conversion and management. 2007 Apr 1;48(4):1238-44.

10. Sui R, Prasianakis NI, Mantzaras J, Mallya N, Theile J, Lagrange D, Friess M. An experimental and numerical investigation of the combustion and heat transfer characteristics of hydrogen-fueled catalytic microreactors. Chemical Engineering Science. 2016 Feb 17;141:214-30.

11. Nadimi E, Jafarmadar S. The numerical study of the energy and exergy efficiencies of the micro-combustor by the internal micro-fin for thermophotovoltaic systems. Journal of Cleaner Production. 2019 Oct 20;235:394-403.

12. Pizza G, Mantzaras J, Frouzakis CE. Flame dynamics in catalytic and non-catalytic mesoscale microreactors. Catalysis Today. 2010 Oct 1;155(1-2):123-30.

13. Zhou J, Wang Y, Yang W, Liu J, Wang Z, Cen K. Combustion of hydrogen–air in catalytic micro-combustors made of different material. International Journal of hydrogen energy. 2009 May 1;34(8):3535-45.

14. Wan J, Yang W, Fan A, Liu Y, Yao H, Liu W, Du Y, Zhao D. A numerical investigation on combustion characteristics of H2/air mixture in a micro-combustor with wall cavities. international journal of hydrogen energy. 2014 May 15;39(15):8138-46.

15. Fan A, Wan J, Liu Y, Pi B, Yao H, Maruta K, Liu W. The effect of the blockage ratio on the blow-off limit of a hydrogen/air flame in a planar micro-combustor with a bluff body. international journal of hydrogen energy. 2013 Aug 30;38(26):11438-45.

16. Di Benedetto A, Di Sarli V, Russo G. Effect of geometry on the thermal behavior of catalytic micro-combustors. Catalysis today. 2010 Oct 1;155(1-2):116-22.

17. Yang WM, Chou SK, Pan JF, Li J, Zhao X. Comparison of cylindrical and modular micro combustor radiators for micro-TPV system application. Journal of Micromechanics and Microengineering. 2010 Jun 22;20(8):085003.

18. Liu L, Zhao L, Fan AW. Effects of wall thickness and material on flame stability in a planar micro-combustor. Journal of Central South University. 2019 Aug 1;26(8):2224-33.

19. Veeraragavan A. On flame propagation in narrow channels with enhanced wall thermal conduction. Energy. 2015 Dec 15;93:631-40.

20. Kang X, Veeraragavan A. Experimental investigation of flame stability limits of a mesoscale combustor with thermally orthotropic walls. Applied Thermal Engineering. 2015 Jun 25;85:234-42.

21. Li J, Wang Y, Shi J, Liu X. Dynamic behaviors of premixed hydrogen–air flames in a planar micro-combustor filled with porous medium. Fuel. 2015 Apr 1;145:70-8.

22. Yang WM, Chou SK, Chua KJ, Li J, Zhao X. Research on modular micro combustor-radiator with and without porous media. Chemical engineering journal. 2011 Apr 1;168(2):799-802.

23. Pan JF, Wu D, Liu YX, Zhang HF, Tang AK, Xue H. Hydrogen/oxygen premixed combustion characteristics in micro porous media combustor. Applied Energy. 2015 Dec 15;160:802-7.

24. Chou SK, Yang WM, Li J, Li ZW. Porous media combustion for micro thermophotovoltaic system applications. Applied Energy. 2010 Sep 1;87(9):2862-7.

25. Bermel P, Ghebrebrhan M, Chan W, Yeng YX, Araghchini M, Hamam R, Marton CH, Jensen KF, Soljačić M, Joannopoulos JD, Johnson SG. Design and global optimization of high-efficiency thermophotovoltaic systems. Optics express. 2010 Sep 13;18(103):A314-34.

26. Gentillon P, Singh S, Lakshman S, Zhang Z, Paduthol A, Ekins-Daukes NJ, Chan QN, Taylor RA. A comprehensive experimental characterisation of a novel porous media combustion-based thermophotovoltaic system with controlled emission. Applied Energy. 2019 Nov 15;254:113721.

27. Kang X, Veeraragavan A. Experimental demonstration of a novel approach to increase power conversion potential of a hydrocarbon fuelled, portable, thermophotovoltaic system. Energy Conversion and Management. 2017 Feb 1;133:127-37.

28. Beder EC, Bass CD, Shackleford WL. Transmissivity and absorption of fused quartz between 0.22 μ and 3.5 μ from room temperature to 1500° C. Applied Optics. 1971 Oct 1;10(10):2263-8.

29. Sathya P, RM SP. Numerical modeling and Simulation of Thermophotovoltaic Cell using COMSOL. In2019 Innovations in Power and Advanced Computing Technologies (i-PACT) 2019 Mar 22 (Vol. 1, pp. 1-5). IEEE Ravindra, N M and Marthi, Sita Rajyalaxmi and Bañobre, Asahe. Radiative Properties of Semiconductors. Morgan & Claypool Publishers. 2017; 2053-2571.

30. Osminkina LA, Gonchar KA, Marshov VS, Bunkov KV, Petrov DV, Golovan LA, Talkenberg F, Sivakov VA, Timoshenko VY. Optical properties of silicon nanowire arrays formed by metal-assisted chemical etching: evidences for light localization effect. Nanoscale research letters. 2012 Dec;7(1):1-6.

31. Incropera FP, Lavine AS, Bergman TL, DeWitt DP. Fundamentals of heat and mass transfer. John Wiley & Sons; 2007

32. Forsberg CH. Heat transfer principles and applications. Academic Press; 2020 Mar 20

33. Cengel Y, Cimbala J. EBOOK: Fluid Mechanics Fundamentals and Applications (SI units). McGraw Hill; 2013 Oct 16

34. Yang WM, Chou SK, Shu C, Xue H, Li ZW. Development of a prototype micro-thermophotovoltaic power generator. Journal of Physics D: Applied Physics. 2004 Mar 17;37(7):1017.

35. Licht A, Pfiester N, DeMeo D, Chivers J, Vandervelde TE. A review of advances in thermophotovoltaics for power generation and waste heat harvesting. MRS Advances. 2019;4(41-42):2271-82.

36. Utlu Z, Önal BS. Examination of thermophotovoltaic GaSb cell technology in low and medium temperatures waste heat. InConf Ser Mater Sci Eng 2018 Feb (Vol. 307, p. 012074).

37. Lu Q, Zhou X, Krysa A, Marshall A, Carrington P, Tan CH, Krier A. InAs thermophotovoltaic cells with high quantum efficiency for waste heat recovery applications below 1000 C. Solar Energy Materials and Solar Cells. 2018 Jun 1;179:334-8.

38. Gupta MS, Elikkottil A, Pesala B. SiO 2 Grating-Based Photonic Structures as Ideal Narrowband Emitter for Solar Thermophotovoltaics Application. In Advances in Energy Research, Vol. 1 2020 (pp. 29-35). Springer, Singapore.

39. Sai H, Yugami H. Thermophotovoltaic generation with selective radiators based on tungsten surface gratings. Applied physics letters. 2004 Oct 18;85(16):3399-401.

40. Gupta MS, Ameen E, Veeraragavan A, Pesala B. Design and Fabrication of Grating-Based Filters for Micro-thermophotovoltaic Systems. InProceedings of the 7th International Conference on Advances in Energy Research (pp. 1113-1119). Springer, Singapore.

41. Silva-Oelker G, Jerez-Hanckes C, Fay P. High-temperature tungsten-hafnia optimized selective thermal emitters for thermophotovoltaic applications. Journal of Quantitative Spectroscopy and Radiative Transfer. 2019 Jul 1;231:61-8.

42. Lenert A, Bierman DM, Nam Y, Chan WR, Celanović I, Soljačić M, Wang EN. A nanophotonic solar thermophotovoltaic device. Nature nanotechnology. 2014 Feb;9(2):126-30.

43. Guazzoni GE. High-temperature spectral emittance of oxides of erbium, samarium, neodymium and ytterbium. Applied Spectroscopy. 1972 Jan;26(1):60-5.

44. Gupta MS, Ameen E, Llobet JR, Veeraragavan A, Pesala B. High contrast grating based thermal emitters for portable thermophotovoltaic systems. InHigh Contrast Metastructures VII 2018 Feb 21 (Vol. 10542, p. 1054217). International Society for Optics and Photonics.

45. Shemelya C, DeMeo DF, Vandervelde TE. Two dimensional metallic photonic crystals for light trapping and anti-reflective coatings in thermophotovoltaic applications. Applied Physics Letters. 2014 Jan 13;104(2):021115.

46. Rahmlow Jr T, Lazo-Wasem J, Gratrix E, Fourspring P, DePoy D. Front surface tandem filters using sapphire (Al2O3) substrates for spectral control in thermophotovoltaic energy conversion systems. KAPL (Knolls Atomic Power Laboratory (KAPL), Niskayuna, NY); 2005 Feb 28.

47. Bierman DM, Lenert A, Chan WR, Bhatia B, Celanović I, Soljačić M, Wang EN. Enhanced photovoltaic energy conversion using thermally based spectral shaping. Nature Energy. 2016 May 23;1(6):1-7.

48. Stelmakh V, Chan WR, Ghebrebrhan M, Soljacic M, Joannopoulos JD, Celanovic I. Fabrication of an omnidirectional 2D photonic crystal emitter for thermophotovoltaics. InJournal of Physics: Conference Series 2016 Nov (Vol. 773, No. 1, p. 012037). IOP Publishing.

49. Wang X, Chan WR, Stelmakh V, Soljacic M, Joannopoulos JD, Celanovic I, Fisher PH. Prototype of radioisotope thermophotovoltaic system using photonic crystal spectral control. InJournal of Physics: Conference Series 2015 (Vol. 660, No. 1, p. 012034). IOP Publishing.

50. Chen YB, Zhang ZM. Design of tungsten complex gratings for thermophotovoltaic radiators. Optics communications. 2007 Jan 15;269(2):411-7.

51. Murikipudi V. N. Surendra Gupta, Elikkottil Ameen, Sreedhar Unnikrishnakurup, Krishnan Balasubramaniam, Ananthanarayanan Veeraragavan, Bala Pesala, "Spectral filtering of sub-bandgap radiation using all-dielectric gratings for thermophotovoltaic applications," J. Photon. Energy 11(1), 015501 (2021).

52. Selvakumar N, Barshilia HC. Review of physical vapor deposited (PVD) spectrally selective coatings for mid-and high-temperature solar thermal applications. Solar energy materials and solar cells. 2012 Mar 1;98:1-23.

53. Chan WR, Bermel P, Pilawa-Podgurski RC, Marton CH, Jensen KF, Senkevich JJ, Joannopoulos JD, Soljačić M, Celanovic I. Toward high-energy-density, high-efficiency, and moderate-temperature chip-scale thermophotovoltaics. Proceedings of the National Academy of Sciences. 2013 Apr 2;110(14):5309-14.

54. Lenert A, Bierman DM, Nam Y, Chan WR, Celanović I, Soljačić M, Wang EN. A nanophotonic solar thermophotovoltaic device. Nature nanotechnology. 2014 Feb;9(2):126-30.